

Supporting Information

Evaluation of Microscopic Origins of Optical Response: Based on Rigorous Atomic Space Tessellating

*Yang Chi**

*School of Chemistry and Chemical Engineering, Qufu Normal University, Qufu
273165, P. R. China*

Corresponding author: yang.chi@hotmail.com

I. Susceptibilities

The following expressions with scissor correction derived within the length-gauge formalism are used to calculate the frequency-dependent SHG susceptibility in an insulator or clean semiconductor at zero temperature^[1],

$$\chi^{abc}(-2\omega; \omega, \omega) = \chi_e^{abc}(-2\omega, \omega, \omega) + \chi_i^{abc}(-2\omega, \omega, \omega), \quad (\text{S1})$$

$$\chi_e^{abc}(-2\omega; \omega, \omega) = \frac{e^3}{\hbar^2 \Omega} \sum_{nm, l, k} \frac{r_{nm}^a \{r_{ml}^b r_{ln}^c\}}{(\omega_{ln} - \omega_{ml})} \times \left[\frac{2f_{nm}}{\omega_{mn} - 2\omega} + \frac{f_{ln}}{\omega_{ln} - \omega} + \frac{f_{ml}}{\omega_{ml} - \omega} \right], \quad (\text{S2})$$

$$\begin{aligned} \chi_i^{abc}(-2\omega; \omega, \omega) = & \frac{i}{2} \frac{e^3}{\hbar^2 \Omega} \sum_{nm, k} f_{nm} \left[\frac{2}{\omega_{mn}(\omega_{mn} - 2\omega)} r_{nm}^a (r_{nm;c}^b + r_{nm;b}^c) + \frac{1}{\omega_{mn}(\omega_{mn} - \omega)} (r_{nm;c}^a r_{mn}^b + r_{nm;b}^a r_{mn}^c) \right. \\ & \left. + \frac{1}{\omega_{mn}^2} \left(\frac{1}{\omega_{mn} - \omega} - \frac{4}{\omega_{mn} - 2\omega} \right) r_{nm}^a (r_{mn}^b \Delta_{mn}^c + r_{mn}^c \Delta_{mn}^b) - \frac{1}{2\omega_{mn}(\omega_{mn} - \omega)} (r_{nm;a}^b r_{mn}^c + r_{nm;a}^c r_{mn}^b) \right]. \end{aligned} \quad (\text{S3})$$

The calculation of the first-order susceptibility tensor adopts a well-known form,

$$\chi_{ab}^{(1)}(-\omega; \omega) = \frac{e^2}{\hbar \Omega} \sum_{n, m, k} \frac{r_{nm}^a r_{mn}^b f_{mn}}{\omega_{nm} - \omega}. \quad (\text{S4})$$

The real part n of the complex refractive index is calculated using the following formula,

$$n(\omega) = \frac{1}{\sqrt{2}} \left[(\varepsilon_1(\omega)^2 + \varepsilon_2(\omega)^2)^{1/2} + \varepsilon_1(\omega) \right]^{1/2}. \quad (\text{S5})$$

II. Space partition methods in the AST scheme

1. Discrete atomic space analysis

There are two most representative methods here, Voronoi^[2] (cell-like) and “the quantum theory of atoms in molecules”^[3] (AIM) partition, which were originally proposed to analyze the charge density of molecules. Both methods are partition space discretely, so any point in Bloch orbital can be attributed to only one atom,

$$\begin{cases} w_A(\mathbf{r}) = 1, & \mathbf{r} \in \Omega_A \\ w_A(\mathbf{r}) = 0, & \mathbf{r} \notin \Omega_A \end{cases},$$

where Ω_A is atomic space of atom A.

Therefore, the sum of all atomic spaces in the unit cell is strictly equal to the unit cell volume (for AIM partitioning, in the absence of pseudoatoms),

$$\sum_i \Omega_A^i = \Omega.$$

The AIM partition adopts a physically meaningful approach, dividing the entire three-dimensional space into atomic basins through the zero-flux surface of electron density, with no electron density gradient lines crossing the interface. These independent spaces correspond to the atomic spaces defined by AIM theory. In contrast, Voronoi atomic spaces rely solely on the crystal structure, forming closed polyhedra through perpendicular bisectors with neighboring atoms. A characteristic of Voronoi atomic spaces is that any point within a Voronoi atomic space is closer to the atom in that space than to any other atom. In other words, any point in three-dimensional space is assigned to the Voronoi atomic space of the nearest atom.

2. Fuzzy atomic space analysis

The Hirshfeld partition^[4] is one of the widely used fuzzy space methods, and subsequently, many other fuzzy space partition methods such as Becke^[5] and Hirshfeld-I^[6] have been proposed. They continuously partition the three-dimensional space, and the atomic spaces divided by these methods overlap with each other. From a three-dimensional perspective, all atoms occupy exactly the same space, which is the entire molecular or crystal space. Any point in the entire three-dimensional space is attributed to any atom, but with different weights for different atoms. All atoms and any point satisfy the following two conditions,

$$\begin{cases} 0 \leq w_A(\mathbf{r}) \leq 1, \quad \forall A \\ \sum_i w_A^i(\mathbf{r}) = 1 \end{cases}.$$

In order to ensure the determinacy of atomic space partitioning and the absence of empirical parameters, Hirshfeld and Hirshfeld-I methods were chosen here.

Hirshfeld atomic space is defined as^[4],

$$w_A^{\text{Hirshfeld}}(\mathbf{r}) = \frac{\rho_A(\mathbf{r})}{\rho^{\text{pro}}(\mathbf{r})},$$

where ρ^{pro} is procrystal electron density, ρ_A denotes spherically averaged atomic electron density in free state.

Given that the Hirshfeld atomic space does not respond to the actual chemical environment around the atom, subsequent methods have been proposed to iteratively adjust the atomic spaces in response to the surrounding environment. These methods are considered more physically meaningful than the Hirshfeld ones. Among the atomic iteration methods, a representative one is the Hirshfeld-I method, which is an important extension of the Hirshfeld method. The atomic charges obtained through this method are more in line with chemical intuition than those obtained by the Hirshfeld method.

Hirshfeld-I atomic space is defined as^[6],

$$w_A^{\text{Hirshfeld-I},n}(\mathbf{r}) = \frac{\rho_A^{n-1}(\mathbf{r})}{\rho_{pro}^{n-1}(\mathbf{r})},$$

$$\rho_A(\mathbf{r}) = \rho_A^{\text{int}(N_A)}(\mathbf{r}) + \left[\rho_A^{\text{int}(N_A)+1}(\mathbf{r}) - \rho_A^{\text{int}(N_A)}(\mathbf{r}) \right] \left[N_A - \text{int}(N_A) \right],$$

where, the notations $\text{int}(N_A)$ to express the integer part of the atomic electronic population was used.

III. Numerical computation

Structural optimization and electronic structure calculations of β -BBO and CSFS were carried out within the framework of density functional theory (DFT) by using the *CASTEP* package^[7]. The generalized gradient approximation (GGA) within the Perdew–Burke–Ernzerhof (PBE)-type exchange-correlation potentials were used throughout this work^[8]. The employed OTFG norm-conserving pseudopotentials of Ba, B, O, Cs, Sb, F, and S treat 5s 5p 6s, 2s 2p, 2s 2p, 5s 5p 6s, 4d 5s 5p, 2s 2p, and 3s 3p as the valence states, respectively. The plane-wave cutoff energy of 1000 eV and the threshold of 5×10^{-7} eV/atom were set for the self-consistent-field convergence of the total electronic energy. The atomic positions were allowed to relax to minimize the internal forces. An excellent convergence of the energy differences (5.0×10^{-6} eV/atom), maximum force (0.01 eV/Å), and maximum displacement (5.0×10^{-4} Å) was implemented in the atomic position optimization (**Table S1**). A $3 \times 3 \times 3$ and a $5 \times 4 \times 9$ Monkhorst–Pack k -point grid in the Brillouin Zone of the primitive cell are chosen and more than 480 and 545 empty bands were involved in the calculations for β -BBO and CSFS, respectively, to ensure the convergence of SHG susceptibilities. As

the scissors correction has a significant impact on the magnitude of the SHG tensor elements, a scissor operator (1.604 and 0.111 eV for β -BBO and CSFS, respectively) was also used to make the energy gap agree with the experimental values (6.57^[9] and 4.76^[10] eV for β -BBO and CSFS, respectively) rigidly.

IV. Linear and nonlinear optical effects in β -BBO

To verify the accuracy of the calculation results, the optical properties of the classical NLO crystal β -BBO were calculated.

Firstly, the linear optical properties of β -BBO were examined, and both the frequency-dependent refractive index and birefringence showed good agreement with experimental results (**Figure S1** and **Table S2**). The AST scheme was employed to investigate the contributions of different atoms and groups to the anisotropy of polarizability (**Table S3**). The AST scheme can divide the contribution of atoms inside the group, and the division results show that the contributions of bridge oxygens (O1 and O2) to $\Delta\chi^{(1)}$ are significantly smaller than that of terminal oxygens (O3 and O4) in B_3O_6 groups (**Figure S2** and **Table S3**). For comparison with other works, the contribution proportions of on-site transitions of Ba to the $\Delta\chi^{(1)}$ were also calculated (0.78% and 3.60% using the AIM and Hirshfeld partitioning, respectively). These values are very small, consistent with conclusions drawn from previous studies^[11].

Next, the SHG related calculation results will be validated. The calculation results of the frequency-dependent SHG response showed that all four nonlinear coefficients matched exceptionally well with the experimental values at different incident wavelengths reported in various literature (**Figure S3** and **Table S4**). The largest SHG tensor element, i.e., χ^{yy} , was investigated using the AST scheme. The SHG response contributions of β -BBO at zero-frequency and under 1064 nm incident light were very close (**Table S5**), which is quite different from the case of CSFS. Through the calculation of the dipole moment component matrix diagram (**Figure S4**),

it was found that the on-site transitions of the B_3O_6 groups contributed significantly to χ^{yyy} (57.19% and 46.10% using the AIM and Hirshfeld partitioning, respectively, at an incident wavelength of 1064 nm), which is consistent with the findings of other literature^[11,12]. Similar to $\Delta\chi^{(1)}$, the contribution of bridge oxygens (O1 and O2) to χ^{yyy} is significantly smaller than that of terminal oxygens (O3 and O4) in B_3O_6 groups (**Figure S2** and **Table S5**), which is consistent with previous research findings^[12].

In summary, this method has achieved highly consistent results with experimental values in calculating both the macroscopic linear and nonlinear optical properties of β -BBO. For microscopic effects, consistent conclusions can be obtained qualitatively with other methods. In more detailed transition composition analysis, there will be significant differences, such as the division of off-site transitions between Ba and B_3O_6 groups, due to differences in methods.

Table S1. Optimized atomic coordinates for β -BBO and CSFS.

Crystals	Atoms	Wyckoff sites	x	y	z
β -BBO ^a	Ba1		0.30521	-0.33094	0.02399
	B1		0.28087	-0.79842	0.42739
	B2		-0.54539	-0.5005	0.67309
	O1	6b	0.18084	-0.67719	0.39823
	O2		-0.58039	-0.37159	0.58659
	O3		0.26319	-0.88226	0.55033
	O4		-0.62863	-0.54983	0.78726
	Sb1		0.32757	0.41357	0.15195
CSFS ^b	Cs1		-0.01385	0.66127	0.13859
	F1		0.13147	0.43736	0.11491
	F2		0.31751	0.33821	-0.17754
	S1	4a	0.1915	0.12873	0.20157
	O1		0.21458	0.55488	0.56345
	O2		0.26233	0.23442	0.2994
	O3		0.07219	0.16073	0.05002
	O4		0.13797	0.06995	0.44142

^a Rhombohedral, $R3c$, $a = b = c = 8.3857 \text{ \AA}$, $\alpha = \beta = \gamma = 96.7015^\circ$ ^[13].

^b Orthorhombic, $Pna2_1$, $a = 9.9759 \text{ \AA}$, $b = 11.6616 \text{ \AA}$, $c = 5.2968 \text{ \AA}$ ^[10].

Table S2. Comparison of the calculated and experimental values of refractive indexes and birefringence of β -BBO at several specific wavelengths.

λ (μm)	Experimental ^[14]			Theoretical		
	n_o	n_e	Δn	n_o	n_e	Δn
0.40466	1.69267	1.56796	0.12471	1.73393	1.61679	0.11714
0.43583	1.68679	1.56376	0.12303	1.72824	1.61270	0.11554
0.46782	1.68198	1.56024	0.12174	1.72354	1.60932	0.11423
0.47999	1.68044	1.55914	0.12130	1.72209	1.60826	0.11383
0.50858	1.67722	1.55691	0.12031	1.71898	1.60602	0.11296
0.54607	1.67376	1.55465	0.11911	1.71572	1.60365	0.11207
0.57907	1.67131	1.55298	0.11833	1.71336	1.60194	0.11142
0.58930	1.67049	1.55247	0.11802	1.71272	1.60147	0.11125
0.64385	1.66736	1.55012	0.11724	1.70977	1.59931	0.11045
0.81890	1.66066	1.54589	0.11477	1.70414	1.59521	0.10893
0.85212	1.65969	1.54542	0.11427	1.70344	1.59468	0.10876
0.89435	1.65862	1.54469	0.11393	1.70267	1.59411	0.10856
1.01400	1.65608	1.54333	0.11275	1.70100	1.59292	0.10808

Table S3. The contribution percentage of each atom in β -BBO to the $\Delta\chi^{(1)}$ or Δn^2 obtained using the AST scheme, at an incident wavelength of 1064 nm.

Atom	Atomic space partitioning of $\Delta\chi^{(1)}$ or Δn^2 (%)	
	AIM	Hirshfeld
Ba1	17.45	24.88
B1	2.49	7.87
B2	1.86	6.05
O1	12.04	9.14
O2	7.68	5.81
O3	30.78	24.40
O4	27.70	21.85

Table S4. Comparison of the calculated and experimental values of SHG susceptibilities of β -BBO (in pm/V), at different incident wavelengths.

λ (μm)		$ d_{113} $	$ d_{222} $	$ d_{311} $	$ d_{333} $
0.532		0.0790	2.9182	0.0560	0.1107
0.852		0.0441	2.2890	0.0375	0.0534
1.064	Cal.	0.0394	2.1778	0.0344	0.0420
1.313		0.0357	2.1022	0.0324	0.0331
1.319		0.0356	2.1011	0.0323	0.0330
0.532		–	2.6 ^[15]	–	–
0.852		–	2.3 ^[15]	–	–
1.064	Exp.	0.03 ^[15]	2.2 ^[15] ; 2.1 \pm 0.1 ^[16] ; 2.2 \pm 0.2 ^[17] ; 2.23 \pm 0.16 ^[18] ; 2.23 \pm 0.18 ^[19]	0.04 ^[15]	0.04 ^[15]
1.313		–	1.9 ^[15]	–	–
1.319		–	1.89 \pm 0.15 ^[19]	–	–

Table S5. The contribution percentage of each atom in β -BBO to the SHG tensor element $\chi^{yyy}(-2\omega; \omega, \omega)$ obtained using the AIM and Hirshfeld partitioning in the AST scheme, at incident photon energies of 0 and 1.17 eV, respectively.

Atom	Atomic space partitioning of $\chi^{yyy}(-2\omega; \omega, \omega)$ (%)			
	AIM		Hirshfeld	
	0 eV	1.17 eV	0 eV	1.17 eV
Ba1	24.29	24.28	31.71	31.71
B1	2.70	2.71	8.81	8.82
B2	2.76	2.76	8.91	8.92
O1	13.06	13.07	8.99	8.99
O2	13.83	13.82	9.63	9.62
O3	21.74	21.76	16.02	16.04
O4	21.62	21.61	15.92	15.91

Table S6. The contribution percentage of each atom in CSFS to the SHG tensor element $\chi^{zz}(-2\omega; \omega, \omega)$ obtained using the AIM partitioning in the AST scheme, at incident light energies of 0 and 2.0 eV, respectively.

Atom	AIM partitioning of $\chi^{zz}(-2\omega; \omega, \omega)$ (%)	
	0 eV	2.00 eV
Cs1	-2.00	1.64
Sb1	91.54	33.36
S1	9.00	2.10
F1	4.09	6.90
F2	2.81	7.46
O1	-10.95	13.30
O2	4.61	11.10
O3	-2.96	12.18
O4	3.87	11.97

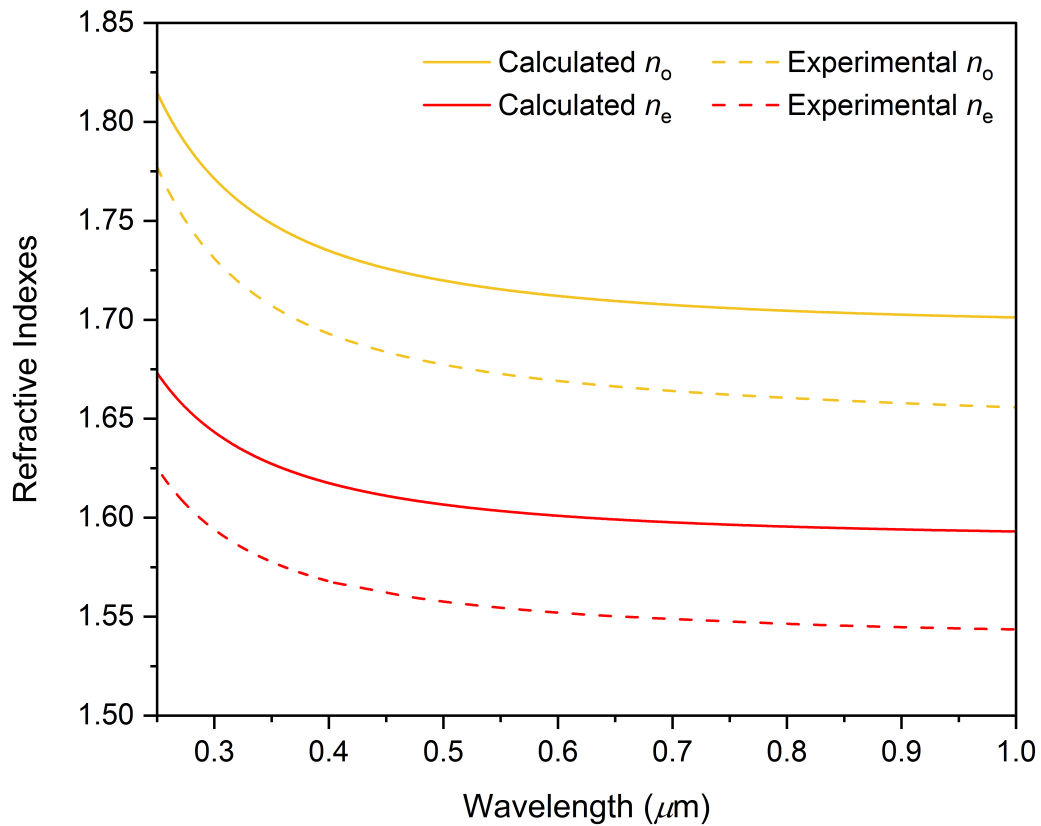


Figure S1. Calculated and experimental dispersion curve of the refractive indexes of β -BBO.

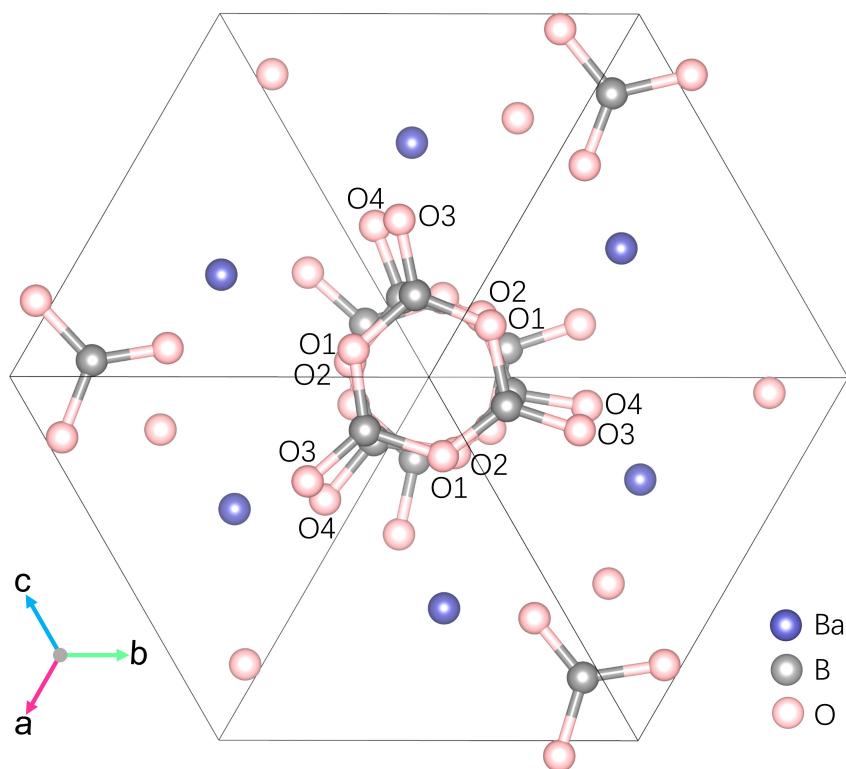


Figure S2. The primitive cell of β -BBO.

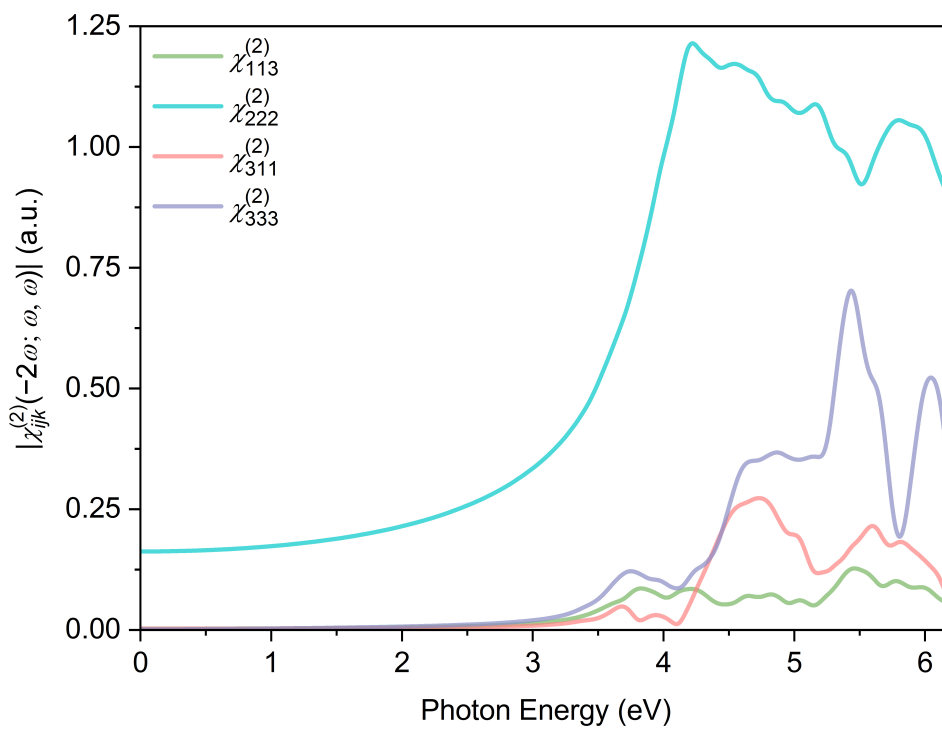


Figure S3. Frequency dependency of $|\chi_{ijk}^{(2)}(-2\omega; \omega, \omega)|$ for β -BBO.

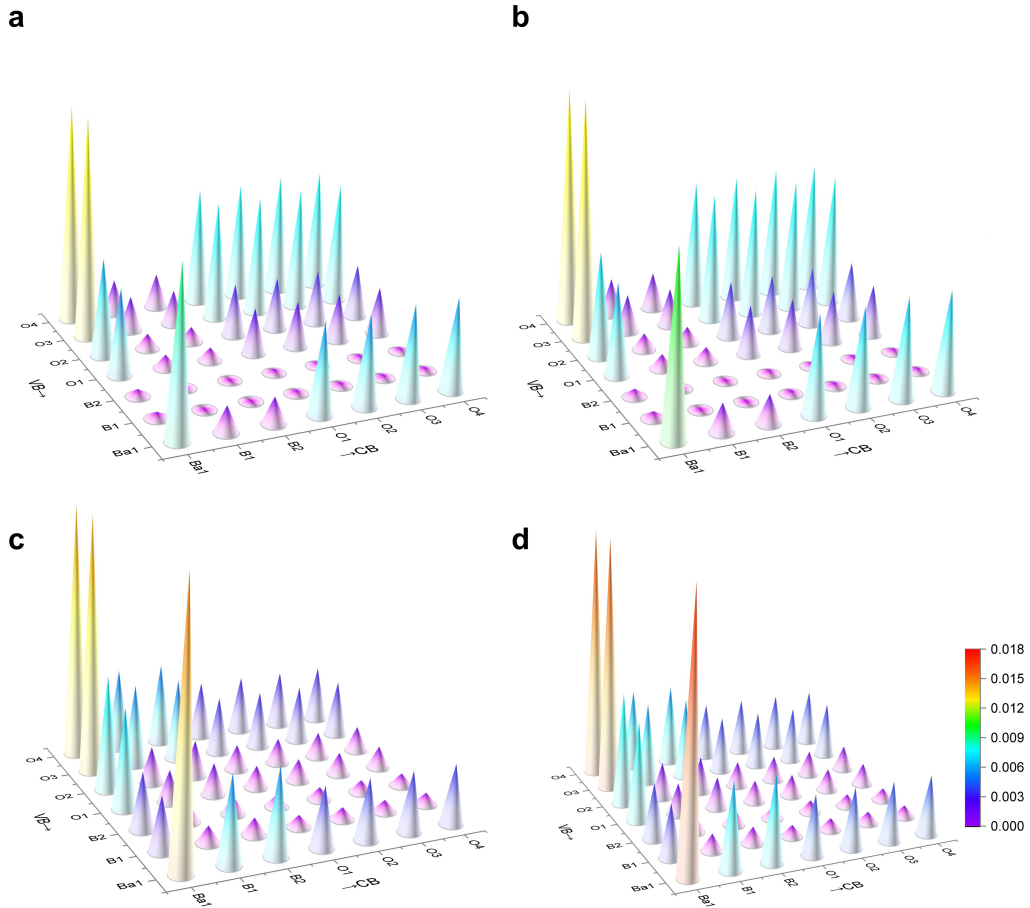


Figure S4. Atomic space dipole moment component matrix diagram of β -BBO for χ^{yyy} at incident photon energies of 0 (**a** and **c**) and 1.17 (**b** and **d**) eV, obtained through two atomic space partitioning methods, i.e., AIM (**a** and **b**), and Hirshfeld (**c** and **d**), respectively. All units are atomic units.

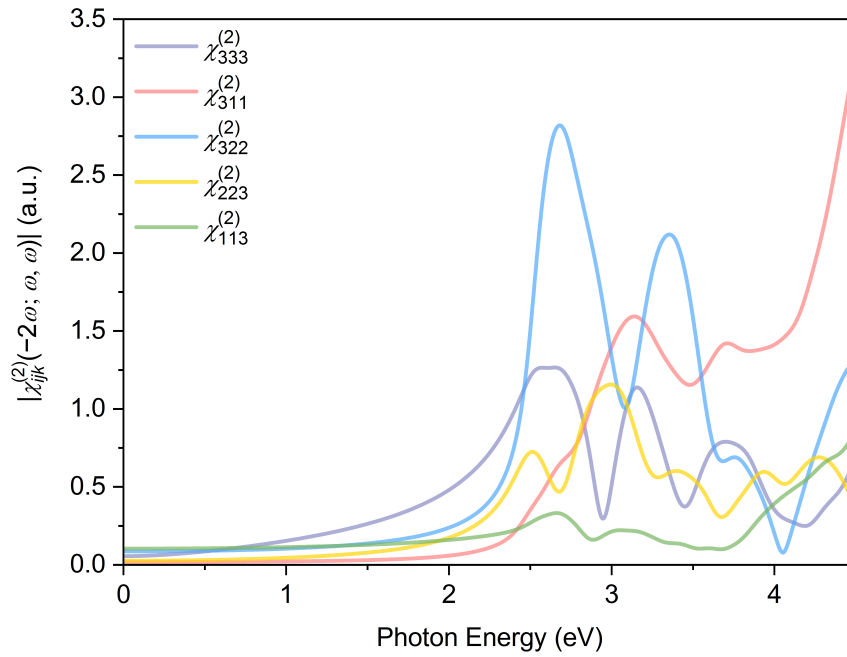


Figure S5. Frequency dependency of $|\chi_{ijk}^{(2)}(-2\omega; \omega, \omega)|$ for CSFS.

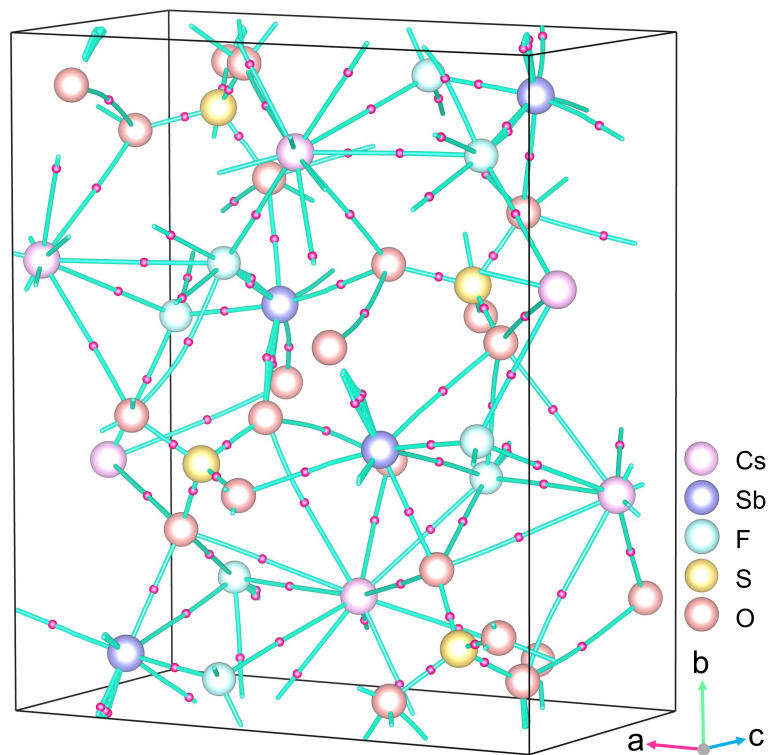


Figure S6. Bond path (green line) and critical point (rose red ball) in CSFS.

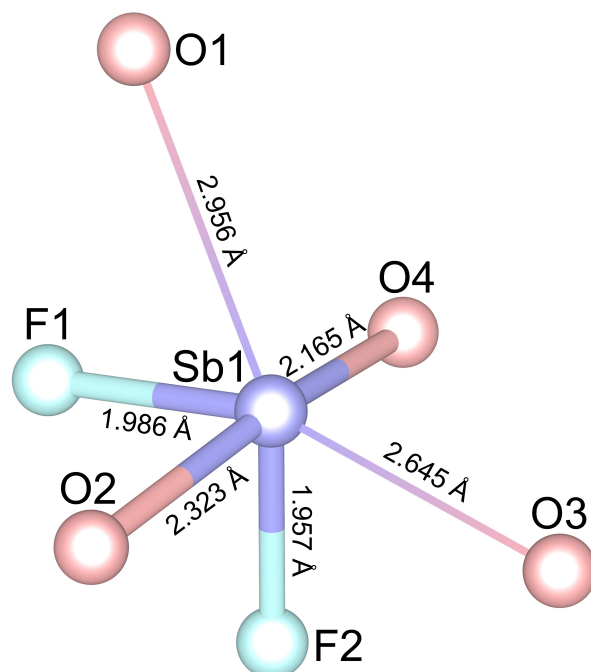


Figure S7. Coordination environment of Sb1 atom in CSFS.

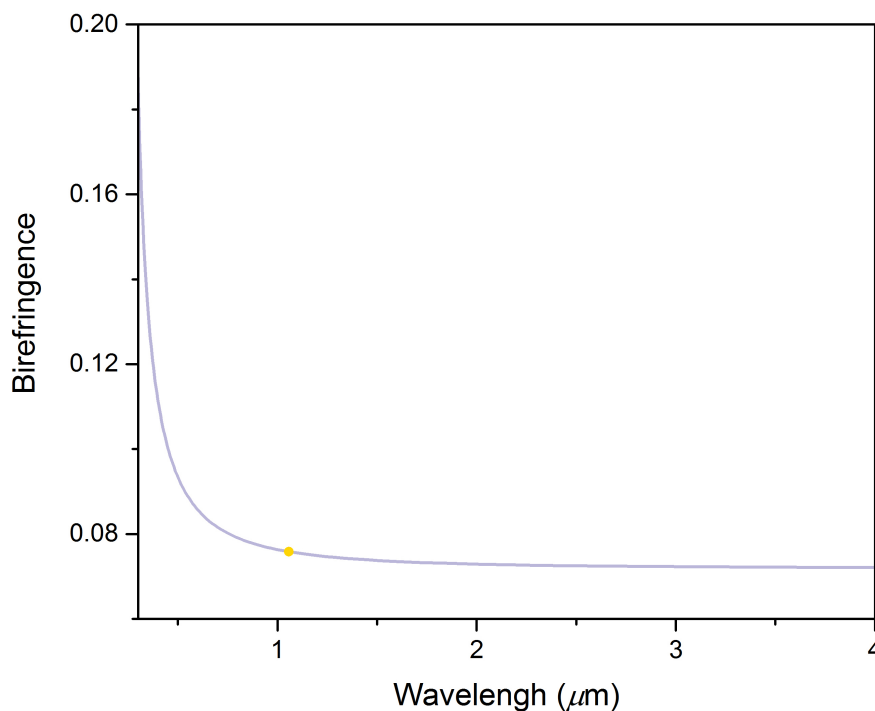


Figure S8. Calculated birefringence of CSFS. The value at 1064 nm is marked with a yellow dot.

References

- [1] F. Nastos, B. Olejnik, K. Schwarz, J. E. Sipe, *Physical Review B* **2005**, *72*, 045223.
- [2] C. F. Guerra, J.-W. Handgraaf, E. J. Baerends, F. M. Bickelhaupt, *J. Comput. Chem.* **2004**, *25*, 189–210.
- [3] a) R. F. W. Bader, P. M. Beddall, *J. Chem. Phys.* **1972**, *56*, 3320–3329; b) R. F. W. Bader, *Atoms in Molecules: A Quantum Theory*. Clarendon, Oxford, **1994**.
- [4] F. L. Hirshfeld, *Theor. Chem. Acc.* **1977**, *44*, 129–138.
- [5] A. D. Becke, *J. Chem. Phys.* **1988**, *88*, 2547–2553.
- [6] P. Bultinck, C. Van Alsenoy, P. W. Ayers, R. Carbó-Dorca, *J. Chem. Phys.* **2007**, *126*, 144111.
- [7] S. J. Clark, M. D. Segall, C. J. Pickard, P. J. Hasnip, M. J. Probert, K. Refson, M. C. Payne, *Z. Kristallogr. - Cryst. Mater.* **2005**, *220*, 567–570.
- [8] J. P. Perdew, K. Burke, M. Ernzerhof, *Phys. Rev. Lett.* **1996**, *77*, 3865.
- [9] R. He, H. W. Huang, L. Kang, W. J. Yao, X. X. Jiang, Z. S. Lin, J. G. Qin, C. T. Chen, *Appl. Phys. Lett.* **2013**, *102*, 231904.
- [10] X. H. Dong, L. Huang, C. F. Hu, H. M. Zeng, Z. E. Lin, X. Wang, K. M. Ok, G. H. Zou, *Angew. Chem., Int. Ed.* **2019**, *58*, 6528–6534.
- [11] J. Lin, M.-H. Lee, Z.-P. Liu, C. T. Chen, C. J. Pickard, *Phys. Rev. B* **1999**, *60*, 13380–13389.
- [12] B.-H. Lei, S. L. Pan, Z. H. Yang, C. Cao, D. J. Singh, *Phys. Rev. Lett.* **2020**, *125*, 187402.
- [13] a) S.-F. Lu, M.-Y. Ho, J.-L. Huang, *Acta Phys. Sin.* **1982**, *31*, 948–955; b) D. F. Xue; S. J. Zhang, *Acta Crystallogr., Sect. B: Struct. Sci.* **1998**, *54*, 652–656.
- [14] D. Eimerl, L. Davis, S. Velsko, E. K. Graham, A. Zalkin, *J. Appl. Phys.* **1987**, *62*, 1968–1983.

- [15] I. Shoji, H. Nakamura, K. Ohdaira, T. Kondo, R. Ito, T. Okamoto, K. Tatsuki, S. Kubota, *J. Opt. Soc. Am. B* **1999**, *16*, 620–624.
- [16] R. S. Klein, G. E. Kugel, A. Maillard, A. Sifi, K. Polgar, *Opt. Mater.* **2003**, *22*, 163–169.
- [17] R. C. Eckardt, H. Masuda, Y. X. Fan, R. L. Byer, *IEEE J. Quant. Electr.* **1990**, *26*, 922–933.
- [18] S. P. Velsko, M. Webb, L. Davis, C. Huang, *IEEE J. Quant. Electr.* **1991**, *27*, 2182–2192.
- [19] W. J. Alford, A. V. Smith, *J. Opt. Soc. Am. B* **2001**, *18*, 524–533.